remote sensing

MDPI

Article

A Study of Lithosphere–Ionosphere Seismic Precursors from Detecting Gamma-Ray and Total Electron Content Anomalies Prior to the 2018 M_L6.2 Hualien Earthquake in Eastern Taiwan

Ching-Chou Fu [1,*], Hau-Kun Jhuang [1,2], Yi-Ying Ho [3], Tsung-Che Tsai [4], Lou-Chuang Lee [1,2,5], Cheng-Horng Lin [1], Ching-Ren Lin [1], Vivek Walia [6] and I-Te Lee [7]

1 Institute of Earth Sciences, Academia Sinica, Taipei 11529, Taiwan; haukunjhuang@alpharing.com (H.-K.J.); louclee@earth.sinica.edu.tw (L.-C.L.); lin@earth.sinica.edu.tw (C.-H.L.); crlin@earth.sinica.edu.tw (C.-R.L.)
2 Alpha Ring Asia Incorporation, Taipei 114066, Taiwan
3 Department of Geosciences, National Taiwan University, Taipei 106319, Taiwan; yiying.ho@gmail.com
4 National Center for High-Performance Computing, NARL, Hsinchu 300092, Taiwan; tctsai@narlabs.org.tw
5 Department of Space Science and Engineering, National Central University, Taoyuan 320001, Taiwan
6 National Center for Research on Earthquake Engineering, NARL, Taipei 106219, Taiwan; walia@ncree.narl.org.tw
7 Taiwan Space Agency, Hsinchu 300091, Taiwan; itlee@tasa.org.tw
* Correspondence: ccfu@earth.sinica.edu.tw; Tel.: +886-2-2783-9910 (ext. 1513); Fax: +886-2-2783-9871

Abstract: This study conducts a comprehensive analysis of observations related to the M_L6.2 Hualien earthquake that struck eastern Taiwan on 6 February 2018, focusing particularly on gamma-ray emissions and total electron content (TEC) as earthquake precursors. Prior research has shown that significant gamma-ray enhancements are frequently detected at the YMSG (Yangmingshan gamma-ray) station prior to major earthquakes in eastern and northeastern Taiwan, suggesting that gamma-ray anomalies may serve as reliable indicators for identifying seismic precursors in this area. Our findings reveal a significant rise in gamma-ray emissions at the YMSG station from 19 January to 4 February 2018, which corresponds to a precursor period of approximately 18 days before the Hualien earthquake. Positive and negative TEC anomalies were observed in Taiwan on 20–21 January and 5 February, respectively, and may be considered as ionospheric precursors to the earthquake. Additionally, deep-learning techniques applied to TEC data facilitate the detection of ionospheric precursors associated with the Hualien earthquake, enabling forecasts of an approaching seismic event. Collectively, these observations indicate that all identified anomalies are regarded as short-term precursors, explicable through the theoretical framework of lithosphere–ionosphere coupling (LIC).

Keywords: gamma-rays; total electron content (TEC); Hualien earthquake; lithosphere–ionosphere coupling (LIC)

check for updates

Academic Editor: Yunbin Yuan

Received: 25 November 2024
Revised: 3 January 2025
Accepted: 6 January 2025
Published: 7 January 2025

Citation: Fu, C.-C.; Jhuang, H.-K.; Ho, Y.-Y.; Tsai, T.-C.; Lee, L.-C.; Lin, C.-H.; Lin, C.-R.; Walia, V.; Lee, I.-T. A Study of Lithosphere–Ionosphere Seismic Precursors from Detecting Gamma-Ray and Total Electron Content Anomalies Prior to the 2018 M_L6.2 Hualien Earthquake in Eastern Taiwan. *Remote Sens.* **2025**, *17*, 188. https://doi.org/10.3390/rs17020188

Copyright: © 2025 by the authors. Licensee MDPI, Basel, Switzerland. This article is an open access article distributed under the terms and conditions of the Creative Commons Attribution (CC BY) license (https://creativecommons.org/licenses/by/4.0/).

1. Introduction

Taiwan is situated at the convergence zone of the Philippine Sea Plate (PSP) and the Eurasian Plate (EP), where the rapid convergence rate of approximately 8 cm/year [1,2] renders the region one of the most seismically active areas globally. Eastern Taiwan, in particular, experiences significant crustal deformation due to the north-northwestward subduction of the PSP beneath the EP. This tectonic interaction induces substantial stress accumulation and deformation, frequently triggering seismic events, particularly in the Hualien region and its surrounding areas. The M_L6.2 Hualien earthquake occurred at

23:50 local time (15:50 UTC) on 6 February 2018. The earthquake's epicenter was located at 121.7°E and 24.1°N, with a focal depth of 6.3 km. The event occurred near the Longitudinal Valley, a prominent north–south trending tectonic feature and a major collision boundary between the Eurasian and Philippine Sea plates. Tectonic activity in this region is characterized by frequent seismicity and crustal deformation, primarily driven by compressive forces between the converging plates and associated fault movements. Given the proximity of the epicenter to Hualien City and the shallow depth of the earthquake, the resulting ground shaking was intense, causing widespread structural damage. Several buildings either tilted or collapsed, leading to numerous fatalities and hundreds of injuries. The mainshock was followed by a sequence of aftershocks, with several significant events occurring in the days immediately following the earthquake [3], heightening public anxiety. These aftershocks were likely a result of stress redistribution as the fault system adjusted in response to the main seismic event. Between October and December 1951, a series of three major seismic events with magnitudes exceeding M_L7 occurred along the Longitudinal Valley, spanning the region between Hualien and Taitung, accompanied by thousands of aftershocks. The 2018 Hualien earthquake sequence is commonly referred to as the 1951 Hualien–Taitung earthquake series [4,5]. The epicenter of the 2018 Hualien earthquake closely aligns with that of the 1951 sequence (Figure 1), underscoring the persistent seismic hazard in this region.

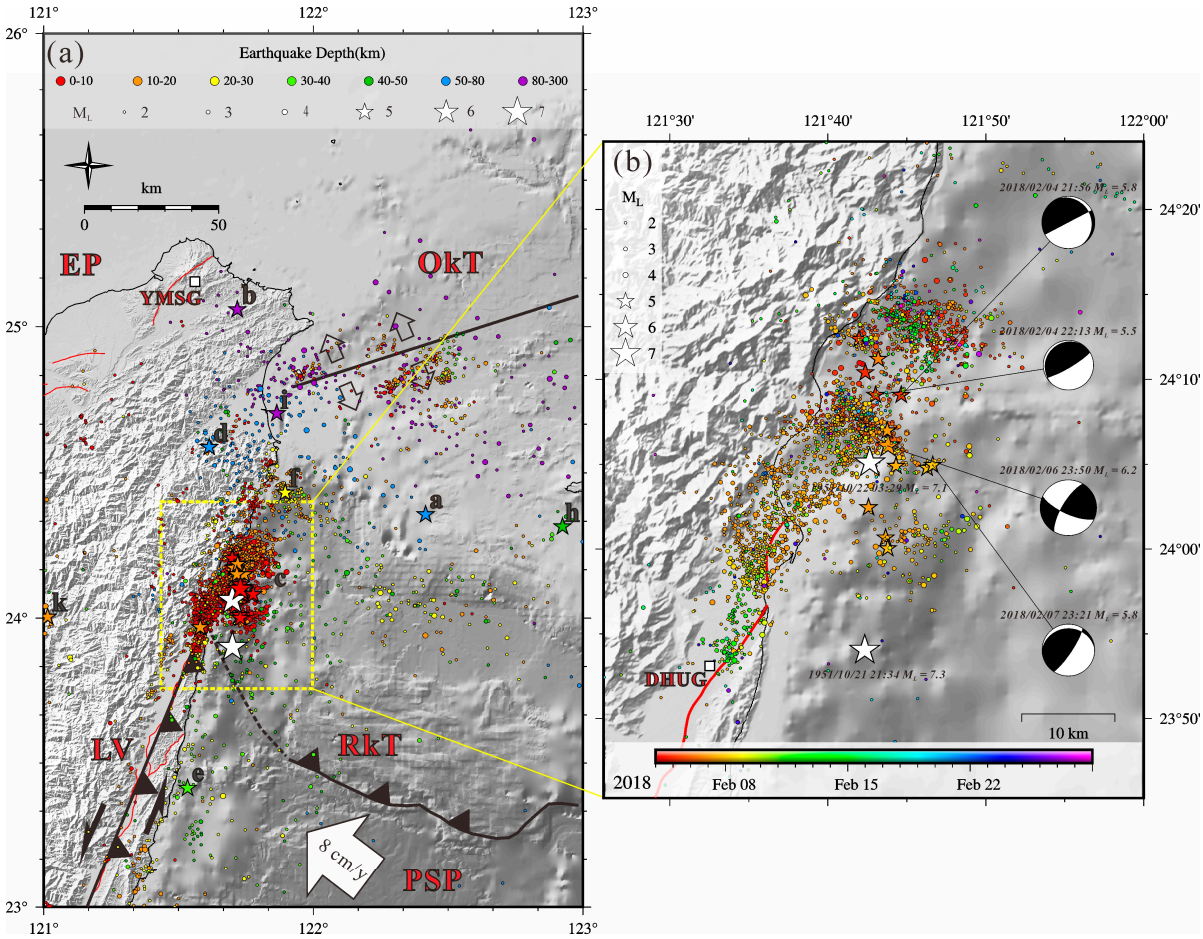


Figure 1. (**a**) The simplified sketch of the regional map and principal tectonic structures around Taiwan shows the Philippine Sea Plate (PSP) is moving northwest at 8 cm/y towards the Eurasia Plate

(EP). In the upper part of Figure 1a, the colored circle symbols represent the earthquake epicenter, with the focal depths corresponding to different colors from 1 December 2017, to 31 March 2018. The open square represents the location of the YMSG gamma-ray station. The red lines indicate the active fault proposed by the Central Geological Survey of Taiwan [6]. The white star indicates the epicenter of the 1951/10/21 (M_L7.3) and 1951/10/22 (M_L7.1) Hualien earthquakes. Seismic events with magnitudes larger than five are labeled and listed in Table 1. (**b**) The circular symbols denote the distribution of aftershock epicenters occurring over a span of approximately three weeks, with variations in color utilized to signify changes in the temporal sequence. LV: Longitudinal Valley; OkT: Okinawa Trough; RkT: Ryukyu Trench.

Table 1. List of gamma-ray anomalies and related earthquakes occurring in Taiwan from 1 December 2017 to 31 March 2018.

No.	Date	Long.	Lat.	Mag.	Depth	Distance	△T	$T_{Duration}$
		(°E)	(°N)	(M_L)	(km)	(km)	(day)	(day)
a	2017/12/08 11:44	122.42	24.36	5.2	79	123.8	3.3	3.5
b	2018/01/17 13:59	121.72	25.06	5.5	140.2	19.0	3.6	3.6
c	2018/02/06 23:50	121.73	24.10	6.2	6.3	118.4	18	16
d	2018/02/19 22:47	121.61	24.59	5.5	52.7	63.2	3.3	1.1
e	2018/02/22 07:10	121.53	23.41	5.6	35.6	193.6	none	none
f	2018/02/26 02:28	121.9	24.43	5.4	22.1	87.2	none	none
g	2018/03/01 21:42	123.92	24.42	5.8	68.3	251.2	none	none
h	2018/03/02 11:42	122.92	24.32	5.3	42.2	166.3	none	none
i	2018/03/06 17:42	121.86	24.7	4.9	81.7	58.8	4.3	1.5
j	2018/03/20 17:22	120.54	23.3	5.3	11.2	230.8	none	none
k	2018/03/29 08:17	121.01	24.0	5.0	11.1	139.3	none	none

The ionospheric total electron content (TEC) has been extensively utilized in the investigation of earthquake precursors and co-seismic propagation phenomena e.g., [7–15]. These studies consistently report that TEC exhibits anomalous variations preceding seismic events. Initial TEC research predominantly utilized data from local global positioning system (GPS) receivers, offering high temporal resolution for localized ionospheric events. In contrast, global ionosphere maps (GIMs) provide a broader spatial context, identifying the location and magnitude of TEC anomalies preceding earthquakes. Zhao et al. [10] pioneered the use of GIM data to observe TEC enhancements three days before the M8.0 Wenchuan earthquake. Similarly, Liu et al. [9] identified TEC anomalies six and three days before the Wenchuan earthquake. Liu et al. [16] expanded on these findings, presenting statistical analyses of 56 $M \geq 6.0$ earthquakes in China, showing that TEC anomalies began to appear 11 days before the events, with GIM-TEC observations centered at 90°E longitude and 35°N latitude. Ho et al. [17] examined the M8.8 Chile earthquake, noting frequent seismo-ionospheric TEC anomalies 10 to 20 days prior to the seismic event. Additionally, Heki [18] and Kuo et al. [15] reported TEC enhancements occurring approximately one hour before several $M \geq 8.0$ earthquakes. Sharma et al. [19] identified a significant TEC anomaly observed two days before the 2010 Mw 7.2 Mexico earthquake, showing a 3–4 TECu deviation and spatial correlation with geological structures near the epicenter. Tachema and Nadji [20] and Nayak et al. [21], using a dense GNSS array approach for ionospheric TEC mapping, reported significant ionospheric density disturbances near the epicenter one week and two weeks before the 2023 Mw 6.8 Moroccan earthquake and the 2016 Mw 6.6 Norcia earthquake, respectively. Haider et al. [22] employed machine learning to analyze ionospheric and atmospheric multi-parameters, identifying multiple earthquake precursors 6–7 days prior to the 2023 Mw 7.8 Turkey earthquake.

Radon (^{222}Rn), a decay product of radium, is generated at a rate of approximately one cubic centimeter per day from ten kilograms of radium. Due to its short half-life of

around 3.82 days, radon is present in the atmosphere at very low concentrations. One of the most notable characteristics of 222Rn is its elevated concentration in fault zones, attributed to the higher porosity of fault regions compared to surrounding rocks. This increased porosity facilitates the migration of gases from deeper crustal layers to the near-surface environment. As a result, 222Rn, along with other soil gases such as CO_2 and helium, is commonly employed in mapping fault systems and monitoring tectonic activity through continuous observation [23–31].

In the lead-up to seismic events, radon may escape from subsurface fractures due to stress-induced changes within the strata, causing observable fluctuations in radon concentrations across various geological settings e.g., [32]. Numerous studies have documented anomalous radon variations in soil gas, hot springs, groundwater, and the atmosphere preceding earthquakes [33–39]. In Taiwan, extensive research on radon emissions in fault zones and deep wells has demonstrated significant increases in radon concentrations prior to earthquakes [25,40–47]. Furthermore, radon decay emits energy in the form of alpha particles, beta particles, and gamma-rays. As a result, the measurement of gamma radiation levels offers an indirect approach to radon detection, providing an effective alternative method for radon monitoring e.g., [48,49].

Previous studies have demonstrated that gamma-ray variations at the DHUG (Dong Hwa University gamma-ray) station are particularly sensitive to earthquake swarms or larger seismic events in the northern segment of the Longitudinal Valley, with epicenters located within 70 km of the station [48]. Similarly, gamma-ray variations at the YMSG (Yangmingshan gamma-ray) station are capable of detecting seismic precursor anomalies for earthquakes with magnitudes exceeding 5 in eastern and northeastern Taiwan, primarily within the area located approximately between latitudes 23.9°N and 25.7°N and longitudes 121.3°E and 122.6°E, exhibiting a notably high detection success rate [49]. On some occasions, gamma-ray levels show a sustained and significant increase days to weeks before an earthquake, followed by a subsequent decrease, with the seismic event occurring as the gamma-ray observed values approach background levels. The 2018 Hualien earthquake fell within the sensitivity range of both the YMSG and DHUG stations, presenting an opportunity to analyze gamma-ray data from these sources. However, the DHUG station was undergoing maintenance during the earthquake due to an instrument malfunction, rendering data from that period unavailable for analysis.

This study integrates gamma-ray and ionospheric TEC observational parameters collected before and after the occurrence of the Hualien earthquake on 6 February 2018. The primary objective of this research is to identify potential earthquake precursors through the analysis of various observational datasets and to propose plausible underlying mechanisms. We believe that the identification of robust precursory indicators specifically tailored to this region could significantly enhance disaster mitigation strategies for future large-scale seismic events.

2. Observations and Methodology

2.1. Gamma-Ray Observation

The gamma-ray monitoring station (25.1544°N, 121.5616°E) is outfitted with a gamma-ray spectrometer featuring a scintillation counter, which is housed within a container composed of 7 cm thick lead and is inserted into a high-density polyethylene (HDPE) tube at a depth of 2 m. The NE110 gamma-ray detector utilized in this setup is a plastic scintillator with dimensions of 400 mm × 400 mm × 400 mm, linked to photomultiplier tubes with diameters of 7.6 cm. The lead container functions as a decay chamber, providing passive shielding that effectively minimizes the influence of cosmic gamma-rays from atmospheric sources and environmental radiation, including decay products, on the scintillation counter.

This design ensures that the observed gamma-ray variations are predominantly attributed to subsurface sources [50]. The operational protocols and setup methodologies for the gamma-ray monitoring station are in accordance with the detailed procedures outlined by Fu et al. [48].

2.2. The Ionospheric Total Electron Content

Previous research on ionospheric earthquake precursors has extensively analyzed TEC data to detect potential anomalies associated with seismic events. These studies commonly focus on identifying whether negative anomalies, characterized by reductions in TEC values below the first quartile, or positive anomalies, defined as enhancements above the third quartile, occur within a 15-day period preceding an earthquake. Such anomalies are considered as potential indicators of precursor activity, aiming to improve the understanding of ionospheric responses to seismic processes. e.g., [9,51]. Given that TEC data are time-series in nature, they are particularly well-suited for the application of recurrent neural networks (RNN), with the long short-term memory (LSTM) model being the most commonly utilized. Tsai et al. [52] employed the bidirectional long short-term memory (Bi-LSTM) model to investigate ionospheric precursors for earthquakes with magnitudes $\geq$ 6.0 in Taiwan from 2003 to 2014, achieving notable accuracy. Accordingly, this study seeks to employ the same approach to detect potential ionospheric precursors for the 2018 Hualien earthquake. A comprehensive discussion of the advanced models and the anomaly detection process is provided by Tsai et al. [52].

The TEC data in this study are obtained from (1) global ionosphere maps (GIMs) and (2) the Center Weather Administration (CWA) in Taiwan. The global GIM-TEC data are provided every 2 h/1 h, with a 2.5° × 5° in latitudinal and longitudinal resolution before/after October 2014. The GIM-TEC data from Center for Orbit Determination Europe (CODE), University of Bern, Switzerland (http://ftp.aiub.unibe.ch/CODE/) was obtained. On the other hand, with more than 150 GPS receivers in the CWA, the CWB-TEC provides high temporal and spatial resolution TEC data every 5 min, achieving a 0.5° × 0.5° latitudinal and longitudinal resolution. In this study, the hourly CWB-TEC data were used.

2.3. Meteorological Records and Earthquake Catalogues

Meteorological data, encompassing atmospheric pressure, temperature, humidity, and hourly precipitation, were sourced from a meteorological station (25.16498°N, 121.53627°E) operated by the CWA of Taiwan, situated approximately one kilometer from the gamma-ray monitoring station. These measurements are recorded hourly and are transmitted wirelessly to the server at the Institute of Earth Sciences, Academia Sinica, integrating data from both the gamma-ray and meteorological monitoring stations (Figure 2). Seismic data were retrieved from the earthquake catalogues maintained by the CWA. During the monitoring period spanning from 1 December, 2017, to 31 March 2018, a total of 500 seismic events with magnitudes ranging from 1.5 to 6.5 were documented in the Taiwan region (Figures 1 and 2).

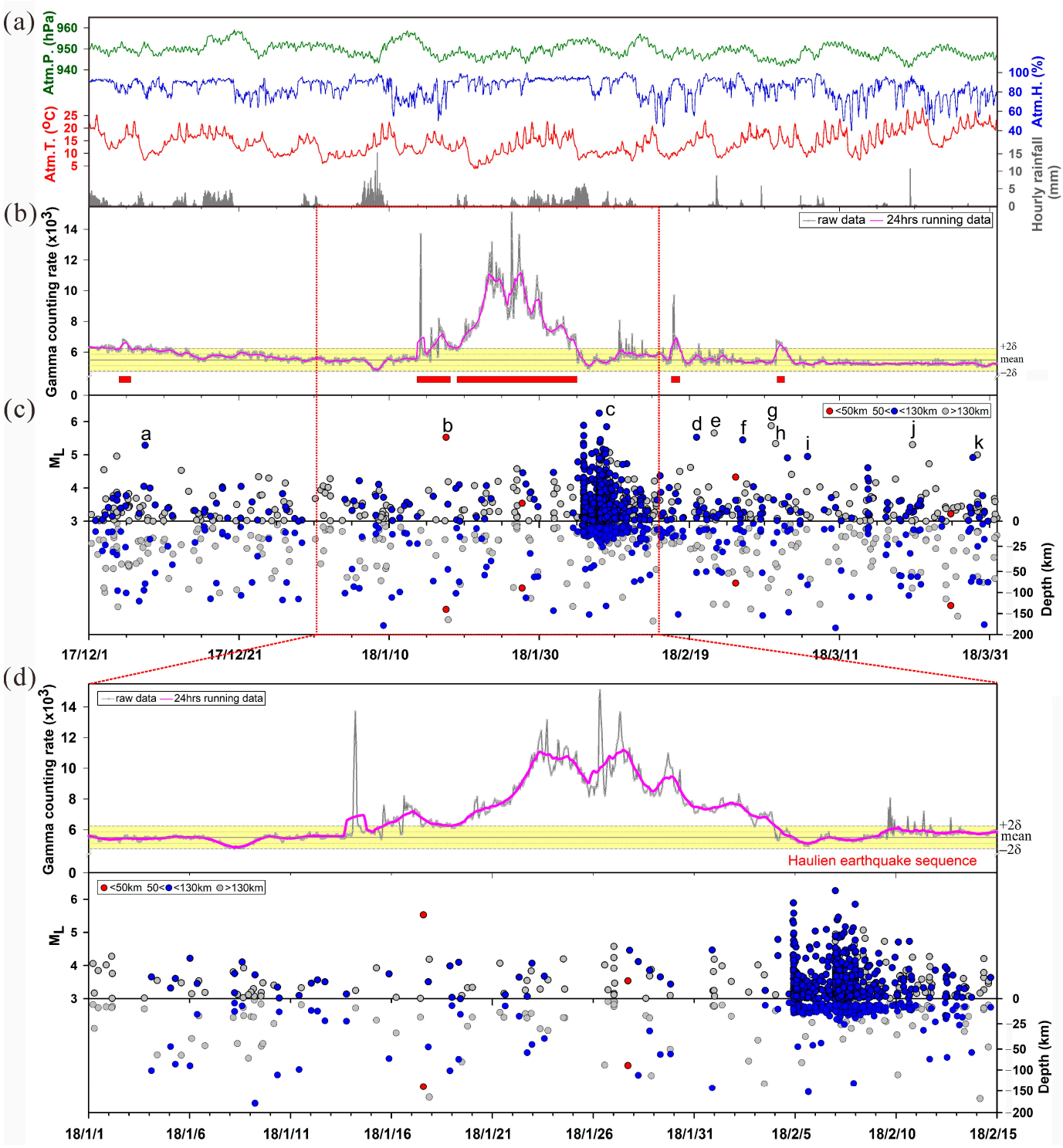


Figure 2. The temporal variations, from 1 December 2017, to 31 March 2018, are displayed for the meteorological data (**a**), including atmospheric pressure (green), humidity (blue), temperature (red), and hourly rainfall (black); the gamma-rays (**b**) where purple lines indicate the 24 h running averages of gamma-ray data, grey lines represent the raw data, horizontal dashed lines indicate the annual averages of the observed results, and the anomalous threshold value (±2σ) is shown with the yellow bar; and the magnitude and depth of earthquakes (**c**) are designated by circle symbols in different colors, denoting the epicenter distance to the YMSG station (i.e., red for <50 km, blue for 50 to 130 km, and grey for >130 km). A zoomed time period (**d**) from 1 January to 14 February 2018, exhibits more details about the gamma-rays and earthquake activity.

3. Results

The gamma-ray results, in conjunction with the meteorological data recorded hourly at the YMSG station for a period from 1 December 2017, to 31 March 2018, are illustrated with seismic events in Figure 2. The gamma counting rate exhibited a variation ranging from 4755 to 15,085 counts per hour (cph), with a mean value of 5489 cph. Concurrently, atmospheric pressure (P_{atm}) fluctuated between 941 and 959 mbar, atmospheric humidity (H_{atm}) ranged from 39 to 100%, and atmospheric temperature (T_{atm}) varied from 2.6 to 25.1 °C, with corresponding mean values of 949 mbar, 84.4%, and 13.1 °C, respectively. Notably, temporal variations in the meteorological factors were not evident. Variations in gamma-rays has been recorded, as shown by the grey line in Figure 2b. The 24 h running average of the gamma counting rate is shown as a purple line to distinguish their corresponding backgrounds. The threshold values are determined using the mean value plus two standard deviations, as shown by the gray dashed lines. Throughout the observation period, the gamma counting rate displayed significant increases at particular intervals, denoted by red bars. The locations of earthquake epicenters and their corresponding depths are presented in Figure 2c. The seismic event dataset, which is required to investigate the spatial distribution of selected seismic events, encompassed both the magnitudes and depths of the earthquakes, which were sorted according to the distances between the YMSG station and the respective earthquake epicenters. Earthquakes are color-coded as red, blue, and gray circles, representing distances of less than 50 km, between 50 and 130 km, and greater than 130 km, respectively. The distribution of specific seismic events is highlighted in Figure 1, including those with magnitudes ≥ 5. Table 1 lists the label of relevant earthquakes indicated in Figures 1 and 2 (first column), the observation data (second column), the geographical coordinates (third and fourth columns), the magnitude (fifth column), the depth (sixth column), the distance to the YMSG station (seventh column), the time difference between the start time of an anomaly and the earthquake occurrence (eighth column), and the duration of gamma-ray anomalies (ninth column). It is important to note that the epicenter of the earthquake that occurred on 2018/03/01 21:42 is located outside the geographical boundaries depicted in Figure 1.

Figure 3 shows an hourly variation of CWA-TEC at latitude 24.0°N and longitude 121.5°E from 25 days before to 25 days after the M_L6.2 Hualien earthquake. The red curve is the observed CWA-TEC. A data gap occurs from 19:00 LT on 26 January 2018 to 23:00 LT on 29 January 2018. Based on [9], we construct the associated upper bound (UB) and lower bound (LB) from the running median ($\widetilde{M}$), lower quartile (LQ), and upper quartile (UQ) for a running period of 15 days before each hourly observation. The lower bound (LB) and upper bound (UB) are given as:

$$LB = \widetilde{M} - 1.5(\widetilde{M} - LQ), \tag{1}$$

$$UB = \widetilde{M} + 1.5(UQ - \widetilde{M}). \tag{2}$$

In Figure 3, the gray curves represent the corresponding LB and UB. When the observed TEC values exceed these bounds, the ten-fold normalized absolute deviations between the observed TEC and $\widetilde{M}$ are displayed as black or red shading in Figure 3. The normalized deviation is defined as:

$$\Delta TEC_n = \frac{|TEC_{obs} - \widetilde{M}|}{TEC_d}, \tag{3}$$

where TEC_d is the daily average value of the observed TEC and TEC_{obs} is the hourly CWA-TEC observed value. The vertical black lines denote the occurrences of M $\geq$ 5.0

earthquakes, where the thick vertical line denotes the M_L6.2 earthquake occurring on 6 February 2018.

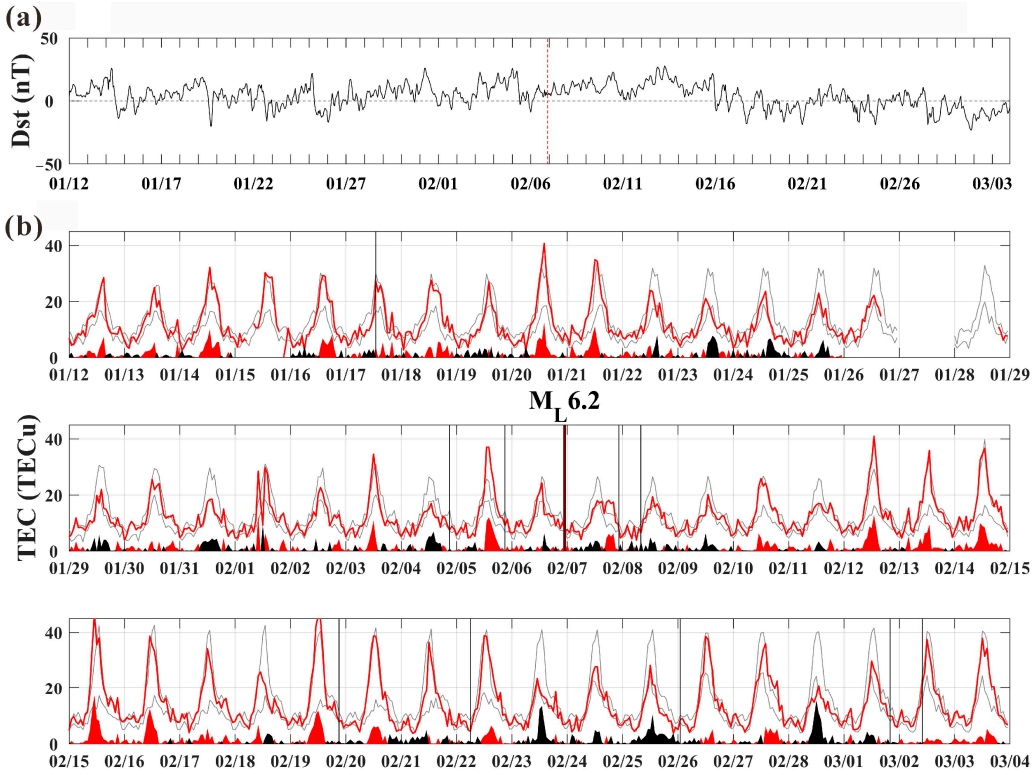


Figure 3. (**a**) Dst index and (**b**) The TEC variation at 24.0°N and 121.5°E from 25 days before to 25 days after the M_L6.2 Hualien earthquake. The red curve is the hourly observed TEC, the two gray curves are the associated UB and LB bounds. The red/black shadow denotes the absolute value of deviations for those observed TEC higher (red) than UB or lower (black) than LB bounds.

Figure 4 displays the observed TEC in red and the predicted TEC in blue, derived from GIM-TEC and CWA-TEC, respectively, as calculated by the trained model, spanning the period from 7 January to 5 February 2018. The hourly GIM-TEC data are obtained at latitude 22.5°N and longitude 120°E for this study (Figure 4a). The predicted TEC is regarded as the normal TEC without the significant influences from earthquakes with M > 5.3. The predicted TEC is evaluated based on deep learning of the input feature data, including GIM-TEC, sunspot number (SSN), F10.7, Lyman-α, and Dst index from the previous 7 days [52]. The normalized deviations, ΔTEC_n (black shadow), are derived from:

$$\Delta TEC_n = |\frac{TEC_{obs} - TEC_{pre}}{TEC_d}|, \quad (4)$$

where TEC_{obs} is the hourly GIM-TEC observed value, TEC_{pre} is the hourly predicted TEC value from the trained model, and TEC_d is the daily average of the GIM-TEC.

The CWA-TEC data obtained from the local GPS receivers of the CWA are shown in Figure 4b. The previous 15-day running median TEC are shown by blue line. The normalized deviation in Figure 4b is determined by:

$$\Delta TEC_n = \frac{|TEC_{obs} - \widetilde{M}|}{TEC_d}, \quad (5)$$

where TEC_{obs} is the hourly CWA-TEC observed value, $\widetilde{M}$ is the running median derived from the previous 15 days CWA-TEC, and TEC_d is the daily average value of the observed

TEC. Although Figure 4b shows a gradual increase in deviations since 11 January, the temporal distribution of these deviations does not align with patterns observed in previous studies on seismic-ionospheric precursors e.g., [51,53]. Consequently, the use of advanced artificial intelligence techniques could provide valuable insights, as detailed in Section 4.2.

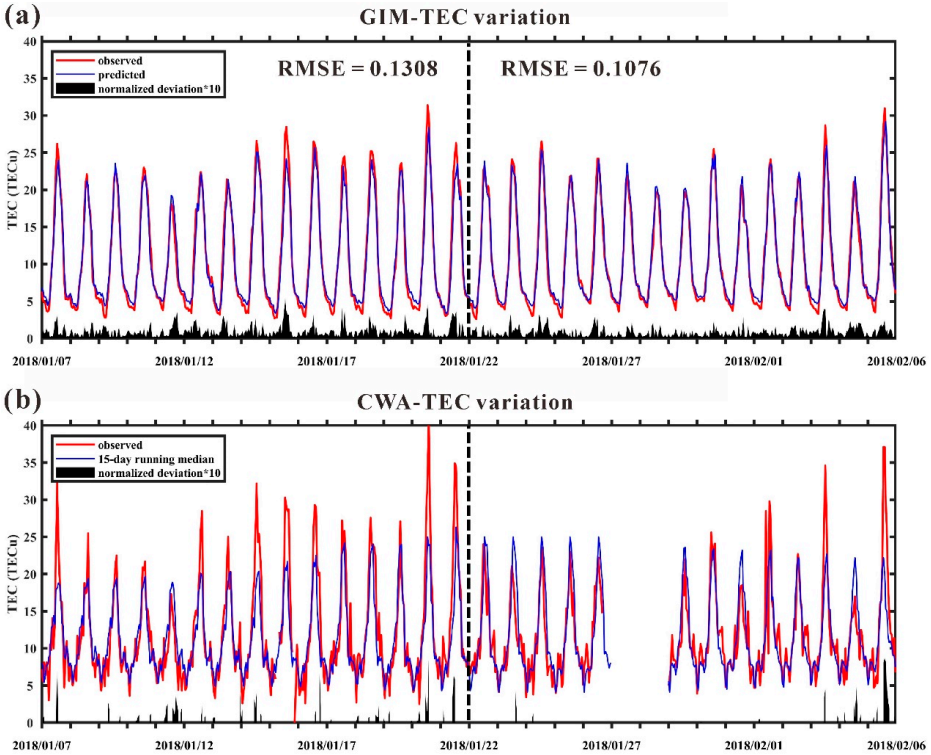


Figure 4. Thirty days of TEC variations before the M_L6.2 Hualien earthquake. (**a**) The GIM-TEC variations, from 7 January to 5 February 2018, where the red line denotes the observed TEC and the blue one designates the predicted TEC from the trained model. The black shadow denotes the absolute value of the normalized deviations between the observed GIM-TEC and predicted TEC. The root mean square error (RMSE) for the period from 7 January to 22 January and 22 January to 5 February is 0.1308 and 0.1076, respectively. (**b**) The CWA-TEC variations from 7 January to 5 February 2018. The red line denotes the observed TEC from CWA data. The blue line denotes the previous 15 days running median of the CWA-TEC data. The black shadow denotes the absolute value of the normalized deviations between the observed CWA-TEC and the running median TEC.

4. Discussion

4.1. The Relationship Between Gamma-Ray Variations and Seismicity

While some studies have suggested that gamma-ray variations may be influenced by meteorological factors [48,54–56], Fu et al. [49] demonstrated that gamma-ray fluctuations at the YMSG station are not significantly impacted by atmospheric pressure, humidity, or temperature. However, short-term heavy rainfall or cumulative precipitation can lead to a temporary and abrupt increase in gamma-rays, which typically returns to background levels within several hours after the rain subsides. As a result, any sustained anomalous variations observed in this study can be regarded as independent of meteorological influences.

Figure 2 illustrates the time series of gamma-ray data recorded at the YMSG station in conjunction with seismic events occurring from 1 December 2017, to 31 March 2018. Notable increases in gamma-ray emissions are observed during specific intervals. In this study, gamma-ray anomalies are defined as precursors when the moving average exceeds two standard deviations, allowing for correlation with seismic events (refer to Figure 4 and Table 1). A comparative analysis of gamma-ray data and earthquakes detected by the

CWA during the monitoring period indicates that, with the exception of five out of the eleven earthquakes with a magnitude ≥ 5 (events e, g, h, j, and k) that occurred at distances exceeding 130 km and Event f, gamma-ray anomalies are typically associated with specific seismic events.

This study consolidates the mainshock of the Hualien earthquake that occurred on 6 February 2018, along with the foreshock of magnitude greater than 5 recorded on 4 February 2018, and the subsequent aftershocks as a singular seismic event, termed the Hualien earthquake sequence (Event c). It is noteworthy that although the magnitude of Event i is slightly below 5, its epicenter is sufficiently proximal and falls within the sensitive detection range of the YMSG station ; hence, this earthquake is considered in this analysis. Throughout the observation period, significant increases in the gamma-ray counting rate were documented at specific intervals, denoted by red bars. Each significant increase in gamma-ray anomalies is associated with a specific earthquake and is generally correlated with precursory anomalous increases occurring a few days (e.g., Events a, b, d, and i) to a few weeks (e.g., Event c) before the corresponding seismic event, referred to as the precursory event (PE). The time occurrences of these precursors and the corresponding seismic features are detailed in Table 1.

An illustrative example is the observations indicating a sudden increase beginning on 14 January 2018, which persisted for approximately three days. Following this, on 17 January, a magnitude 5.5 earthquake with a focal depth of approximately 140 km was recorded near the Tatun Volcanic Group (Event b). Another notable case is the pre-earthquake anomalous period of gamma-rays recorded from 19 January to 3 February 2018, preceding the Hualien earthquake (Event c). The gamma-ray emissions exhibited a gradual increase, culminating in a peak value of approximately 12,000 counts per hour (cph) on 27 January 2018. Following this peak, a gradual decline in the gamma-ray counting rate was observed from 27 January to 3 February 2018, returning to background levels before the occurrence of Event c. This substantial variation in gamma-ray emissions was identified as a precursor, with a precursory time of approximately 18 days prior to the Hualien earthquake on 6 February 2018 (Figure 2d). Anomalous radon emissions are likely linked to tectonic stress, particularly during the earthquake preparation phase, when fault zones exhibit abnormal emissions driven by the accumulation of tectonic stress [27,57]. Elevated radon exhalation rates and concentrations are frequently associated with increased stress and energy storage along fault boundaries, resulting in fractures and heightened crustal permeability. Notably, radon concentrations typically demonstrate a gradual decline preceding an earthquake, a behavior consistent with the findings of this study [25,49,58,59].

In this context, $\triangle$T, referred to as the precursory time, represents the time interval between the onset of an anomaly and the subsequent earthquake event. Consequently, upon excluding the five earthquake events (Events e, g, h, j, and k) that lie outside the sensitive detection range of the YMSG station, five out of the six earthquakes exhibit anomalous signals, resulting in a high success rate.

Figure 5a illustrates the correlation between the magnitude of the PE and precursory time delay (ΔT, representing the time difference between the onset of an anomaly and the corresponding earthquake event for gamma-ray anomalies). The precursory time delay of gamma-ray anomalies is found to correlate with larger impending earthquakes, suggesting the potential to estimate the magnitude of future seismic events [49]. Notably, Event c falls near the best-fit line, supporting previous observations at the YMSG station. This implies that if prolonged gamma-ray anomalies, particularly those lasting more than two weeks, are detected at the station in the future, there is a significant probability of a magnitude 6 or greater earthquake occurring within the YMSG station's sensitive detection range. Figure 5b shows the relationship between the epicentral distance from the YMSG station

and the magnitude of the PE, indicating that larger impending seismic events tend to have epicenters located farther from the YMSG station, as is the case of Event c.

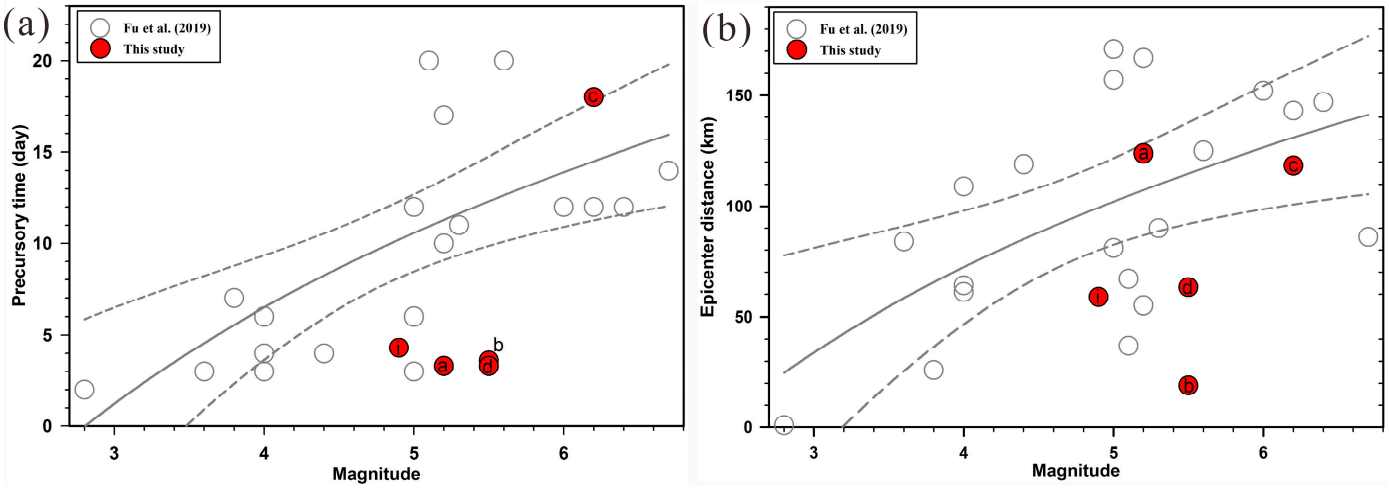


Figure 5. The variation diagrams illustrate the relationship between the magnitude of the precursory event and (**a**) the distribution of precursory time and (**b**) epicenter distance from the YMSG station. The red circles represent the findings of this study. The fitted curves are shown as solid lines, with dashed lines representing the 95% confidence interval of the dataset, and hollow circles correspond to the data from Fu et al. [49].

4.2. The Relationship Between Ionospheric Total Electron Content (TEC) Variations and Seismicity

Figure 3 reveals several significant anomalies exceeding 5–10 TECu, notably on 20 January, 21 January, and 5 February, characterized by the largest positive anomalies (red), whereas the most substantial negative anomalies (black shadow) were observed on 28 February. During the observation period, no significant fluctuations associated with geomagnetic storms were detected, making these short-term, recurrent anomalies plausible precursors to seismic activity e.g., [51]. Notably, ionospheric anomalies began on 20 and 21 January, coinciding with a significant increase in gamma-ray levels, further supporting the connection between these ionospheric irregularities and the 2018 Hualien earthquake. Additionally, slight positive ionospheric anomalies were observed on 14 and 16 January, coinciding with the detection of gamma-ray anomalies during the same period. These observations may be associated with Event b. In Table 1, other earthquakes associated with gamma-ray anomalies, with focal depths exceeding 50 km or magnitudes $\leq$ M5.4, did not exhibit significant TEC anomalies, consistent with the findings of Liu et al. [53].

In recent years, AI (artificial intelligence) techniques such as machine learning and deep learning have become instrumental in earthquake prediction by analyzing extensive TEC and seismic signal data to identify early warning patterns e.g., [52,60,61]. To further investigate whether or not the TEC anomalies were related to the Hualien earthquake, this study also utilized deep-learning-based AI models to detect observed seismo-ionospheric anomalies. Tsai et al. [52] noted a consistent model error between predicted and observed TEC values, typically manifesting around daily peaks and valleys. As shown in Figure 4a, the normalized deviations began to rise on 11 January, concluding on 21 January. On 11 January, the daily peak of the observed GIM-TEC was lower than its predicted counterpart, while the observed daily valley was also considerably lower than the predicted GIM-TEC for that day, indicating a significant discrepancy relative to other days. Beginning 13 January, the daily peak of the observed GIM-TEC surpassed the predicted GIM-TEC, a trend that persisted until 21 January. The root mean square error (RMSE) from 7 January to 22 January was 0.1308, significantly higher than the RMSE of 0.1076 for the period from 22 January to 5 February. Given that the relative error, RE_{RMSE} (0.1774), for the two periods

exceeds the predefined threshold of 0.15 [52], the training model forecasts the occurrence of an M $\geq$ 6.0 earthquake on 6 February, the day following the second period. Figure 4b shows similar trends in the CWA-TEC results, where the normalized deviations began to increase on 11 January and concluded on 21 January. However, due to data gaps observed during the study period (27 January to 28 January) and the absence of a sufficiently long-term CWA-TEC dataset required to develop a dedicated training model for deep learning, this study was unable to utilize CWA-TEC data for earthquake prediction at this stage.

Thus, this study successfully detected seismo-ionospheric anomalies by employing two methodological approaches to assess the temporal TEC variations, providing evidence of potential earthquake precursors for the 2018 Hualien earthquake.

4.3. Summary of Different Anomalies Associated with the 2018 Hualien Earthquake and Its Possible Mechanism

Some studies have documented possible precursory or co-seismic changes associated with the Hualien earthquake. For instance, outgoing longwave radiation (OLR), emitted by the Earth as electromagnetic radiation, is highly sensitive to near-surface and atmospheric temperatures [62]. This sensitivity makes OLR a valuable parameter for monitoring thermal anomalies in seismically active regions through satellite-based analyses. Fu et al. [63] investigated M $\geq$ 6.0 earthquakes from 2009 to 2019 in Taiwan and observed that OLR precursory anomalies generally occur 2–15 days before seismic events. For the 2018 Hualien earthquake, OLR anomalies can be found 14–15 days prior, near the epicenter. In addition, the b-value of the Gutenberg–Richter law [64], a key statistical parameter in earthquake time series, reflects the frequency relationship between large and small earthquakes. A declining b-value is frequently identified as a precursor to major seismic events. Chan et al. [65] investigated the spatiotemporal variations in b-values preceding M $\geq$ 6.0 earthquakes in Taiwan, revealing a marked decline in b-values approximately one year prior to the 2018 Hualien earthquake, underscoring the potential for long-term seismic precursor monitoring. Similarly, Chen et al. [66] examined the earthquake magnitude–frequency relation and identified a significant decrease in b-values two days before the 2018 Hualien earthquake, suggesting a link between b-value anomalies and the distribution of foreshocks in the epicentral region. Additionally, Chen et al. [67] reported that the strong ground motion generated by the 2018 Hualien earthquake induced co-seismic geomagnetic fluctuations and atmospheric disturbances.

This study provides a comprehensive analysis of various observations related to the 2018 Hualien earthquake. Significant changes were first detected at the YMSG station approximately 18 days prior to the event (starting on 19 January), where gamma-rays exhibited a substantial increase that persisted until just before the earthquake. Additionally, notable positive ionospheric anomalies were observed 16–17 days (20–21 January) and one day (5 February) before the earthquake. Abnormal fluctuations in OLR were also recorded around 14–15 days prior to the event (22–23 January). The aforementioned observations are synthesized and presented in the comparative plot in Figure 6.

Based on the results discussed above, a plausible explanation is that the accumulation of tectonic stress prior to an earthquake induces the formation of new fractures in the lithosphere, facilitating the migration of gases and fluids. This process leads to the continuous release of radiogenic gases, such as gamma-rays or radon, from the crustal components [25,49]. Concurrently, the ionization of near-surface air and latent heat exchange contribute to thermal variations [62,63]. Additionally, changes in rock permeability and conductivity, driven by stress accumulation, are induced by electric fields generated by dynamo currents originating in the lithosphere or lower atmosphere. These currents, carrying positive hole charge carriers, flow upwards, altering the electric field in the ionosphere [68–72]. These precursory observations align with the pre-earthquake generation

process, supporting a positive correlation consistent with the lithosphere–atmosphere–ionosphere coupling (LAIC) model [57,71] or lithosphere–ionosphere coupling (LIC) [73], as presented in Figure 6.

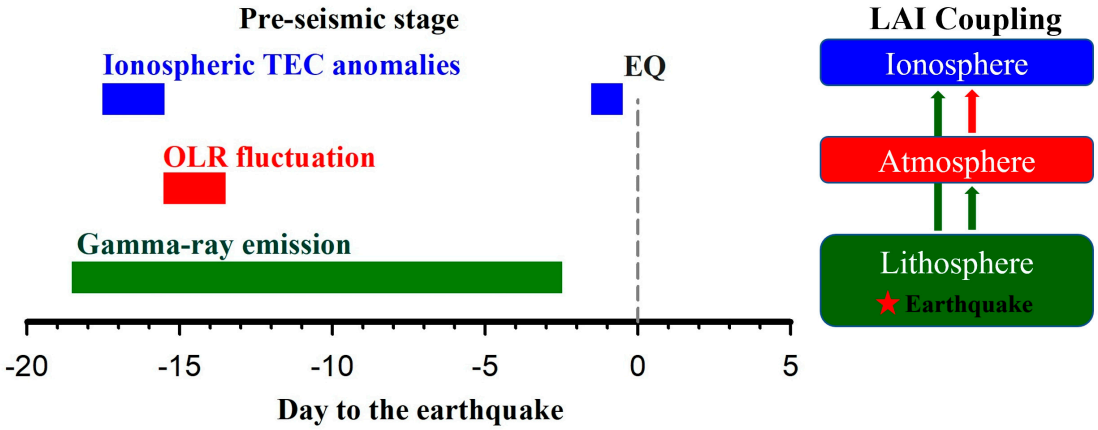


Figure 6. Composite plots of anomalies from multiple observations associated with the 2018 Hualien earthquake and its schematic of the Lithosphere–Atmosphere–Ionosphere (LAI) coupling. Detailed descriptions of each anomaly are provided in the text.

Fu et al. [49] proposed that the YMSG station is situated at the western end of the subduction system in northern Taiwan, where the PSP subducts northward beneath the EP. Due to ongoing plate convergence, pre-seismic slow slip may occur in the vicinity of the subduction zone prior to an earthquake, resulting in volumetric expansion around the EP in northern Taiwan. This expansion leads to the formation of new fractures beneath the YMSG station, facilitating the migration of gas and fluids, which, in turn, releases additional radiogenic gases, such as gamma-rays, from the crustal components. Consequently, gamma-ray variations at the YMSG station may be linked to the dynamics of the subduction process, resembling pre-seismic slow slip phenomena [74]. During the subduction of the PSP, dehydration triggers fluid migration along the subduction interface and vertically through the overlying plate, thereby inducing seismicity [75]. Therefore, the observed earthquake may have been initiated by fault activity within the subduction system off the coast of Hualien. Although the 2018 Hualien earthquake caused significant ruptures along the Milun Fault and Lingding Fault, these faults may not have been the primary triggers of the Hualien earthquake sequence. Kuo-Chen et al. [3] and Lee et al. [76], based on aftershock distribution and joint source inversion analysis, also concluded that the 2018 Hualien earthquake was an event independent of the Ryukyu subduction zone, with subsequent activity triggering the Milun and Lingding faults.

5. Conclusions

This study provides a comprehensive analysis of observational data from the 2018 Hualien earthquake, confirming the effectiveness of gamma-ray and total electron content (TEC) anomalies as earthquake precursors. The major findings and suggestions of this study are listed below:

1. A significant increase in gamma-rays was observed at the YMSG station approximately 18 days before the earthquake, persisting until the event occurrence.
2. Ionospheric anomalies were observed 16–17 days and 1 day prior to the earthquake. Additionally, the deep-learning technique positively predicted that the Hualien earthquake would occur on 6 February.
3. These findings support the feasibility of using gamma-ray and TEC anomalies as short-term earthquake precursors, consistent with the LIC model.

4. Our results are in agreement with the work of Fu et al. [49], making evident the important capability of the YMSG station to detect and to forecast large earthquakes within its detection range. Furthermore, the study validates the research conducted by Tsai et al. [52], which employed deep-learning techniques to analyze TEC anomalies, confirming the potentiality of this method for earthquake forecasting.
5. This research underscores the importance of integrating multiple observational indicators to enhance disaster mitigation strategies for future large-scale seismic events.
6. We propose the installation of additional gamma-ray or radon observation stations to enhance spatial coverage, enabling a detailed investigation of potential precursor variations in high-seismic-risk regions across diverse tectonic settings in Taiwan. Furthermore, implementing a deep-learning analysis framework, as demonstrated by Tsai et al. [52], utilizing CWA-TEC data, could achieve high-resolution regional TEC variations. Integrating this approach with ground-based observations and satellite remote sensing data offers a comprehensive methodology for advancing the understanding of earthquake precursors.

Author Contributions: C.-C.F. and H.-K.J. led this project, created figures, conducted data interpretation, and authored the manuscript. Y.-Y.H. and T.-C.T. were responsible for data analysis. L.-C.L., C.-H.L., C.-R.L. and V.W. participated in discussions on data interpretation. I.-T.L. were responsible for data resources. All authors have read and agreed to the published version of the manuscript.

Funding: The research is supported by grants MOST 109-2116-M-002-031, MOST 109-2628-M-001-002-MY3, and NSTC 112-2628-M-001-005, and also NSTC 113-2116-M-001-017, which is funded through the National Science and Technology Council (NSTC), and MOTC-CWB-108-E-01, from the Center Weather Administration of Taiwan.

Data Availability Statement: The data used to support the findings of this study are available from the corresponding author upon request.

Acknowledgments: We are grateful to Kou-Wei Wu and Kou-Hang Chen for the aid in the operation and maintenance of the monitoring station. We thank the National Center for High-performance Computing (NCHC) for providing computational and storage resources. The TEC contribution number for this article is 00195.

Conflicts of Interest: Authors Hau-Kun Jhuang and Lou-Chuang Lee were employed by the company Alpha Ring Asia Incorporation. The remaining authors declare that the research was conducted in the absence of any commercial or financial relationships that could be construed as a potential conflict of interest.

References

1. Yu, S.B.; Chen, H.Y.; Kuo, L.C. Velocity field of GPS stations in the Taiwan area. *Tectonophysics* **1997**, *274*, 41–59. [CrossRef]
2. Yen, J.Y.; Lu, C.H.; Chang, C.P.; Hooper, A.j.; Chang, Y.H.; Liang, W.T.; Chang, T.Y.; Lin, M.S.; Chen, K.S. Investigating active deformation in the northern Longitudinal Valley and city of Hualien in eastern Taiwan using persistent scatterer and small-baseline SAR interferometry. *Terr. Atmos. Ocean. Sci.* **2011**, *22*, 291–304. [CrossRef]
3. Kuo-Chen, H.; Guan, Z.K.; Sun, W.F.; Jhong, P.Y.; Brown, D. Aftershock Sequence of the 2018 Mw 6.4 Hualien Earthquake in Eastern Taiwan from a Dense Seismic Array Data Set. *Seismol. Res. Lett.* **2019**, *90*, 60–67. [CrossRef]
4. Cheng, S.N.; Yeh, Y.T.; Yu, M.S. The 1951 Taitung earthquake in Taiwan. *J. Geol. Soc. China* **1996**, *39*, 267–285.
5. Cheng, S.N.; Yu, T.T.; Yeh, Y.T.; Chang, Z.S. Relocation of the 1951 Hualien, Taitung earthquake sequence, conference on weather analysis and forecasting. In *Proceedings of the Marine Meteorology and Seismology*; Commemoration of 100 Years of Weather Observation in the Taiwan Area; Central Weather Bureau: Taipei City, Taiwan, 1997; pp. 690–699.
6. Lin, C.W.; Chang, W.C.; Lu, S.T.; Shih, T.S.; Huang, W.C. An introduction to the active faults of Taiwan. *2nd Ed. Spec. Publ. Cent. Geol. Survey* **2000**, *13*, 1–122. (In Chinese)
7. Liu, J.Y.; Chen, Y.I.; Chuo, Y.J.; Tsai, H.F. Variations of ionospheric total electron content during the Chi-Chi Earthquake. *Geophys. Res. Lett.* **2001**, *28*, 1383–1386. [CrossRef]

8. Liu, J.Y.; Chuo, Y.J.; Shan, S.J.; Tsai, Y.B.; Chen, Y.I.; Pulinets, S.A.; Yu, S.B. Pre-earthquake ionospheric anomalies registered by continuous GPS TEC measurements. *Ann. Geophys.* **2004**, *22*, 1585–1593. [CrossRef]
9. Liu, J.Y.; Chen, Y.I.; Chen, C.H.; Liu, C.Y.; Chen, C.Y.; Nishihashi, M.; Li, J.Z.; Xia, Y.Q.; Oyama, K.I.; Hattori, K.; et al. Seismoionospheric GPS total electron content anomalies observed before the 12 May 2008 Mw7.9 Wenchuan earthquake. *J. Geophys. Res.* **2009**, *114*. [CrossRef]
10. Zhao, B.; Wang, M.; Yu, T.; Wan, W.; Lei, J.; Liu, L.; Ning, B. Is an unusual large enhancement of ionospheric electron density linked with the 2008 great Wenchuan earthquake? *J. Geophys. Res.* **2008**, *113*, 1–6. [CrossRef]
11. Jhuang, H.K.; Ho, Y.Y.; Kakinami, Y.; Liu, J.Y.; Oyama, K.I.; Parrot, M.; Hattori, K.; Nishihashi, M.; Zhang, D. Seismo-ionospheric anomalies of the GPS-TEC appear before the 12 May 2008 magnitude 8.0 Wenchuan Earthquake. *Int. J. Remote Sens.* **2010**, *31*, 3579–3587. [CrossRef]
12. Heki, K.; Enomoto, Y. Preseismic Ionospheric Electron Enhancements Revisited. *J. Geophys. Res.* **2013**, *118*, 6618–6626. [CrossRef]
13. Le, H.; Liu, L.; Liu, J.Y.; Zhao, B.; Chen, Y.; Wan, W. The ionospheric anomalies prior to the M9.0 Tohoku-Oki earthquake. *J. Asian Earth Sci.* **2013**, *62*, 476–484. [CrossRef]
14. Su, Y.C.; Liu, J.Y.; Chen, S.P.; Tsai, H.F.; Chen, M.Q. Temporal and spatial precursors in ionospheric total electron content of the 16 October 1999 Mw7.1 Hector Mine earthquake. *J. Geophys. Res.* **2013**, *118*, 6511–6517. [CrossRef]
15. Kuo, C.L.; Lee, L.C.; Heki, K. Preseismic TEC changes for Tohoku-Oki earthquake: Comparisons between simulations and observations. *Terr. Atmos. Ocean. Sci.* **2015**, *26*, 63–72. [CrossRef]
16. Liu, J.Y.; Chen, C.H.; Tsai, H.F.; Le, H. A Statistical Study on Seismo-Ionospheric Anomalies of the Total Electron Content for the Period of 56 $M \geq 6.0$ Earthquakes Occurring in China During 1998–2012. *Chin. J. Space Sci.* **2013**, *33*, 258–269. [CrossRef]
17. Ho, Y.Y.; Jhuang, H.K.; Su, Y.C.; Liu, J.Y. Seismoionospheric anomalies in total electron content of the GIM and electron density of DEMETER before the 27 February 2010 M8.8 Chile earthquake. *Adv. Space Res.* **2013**, *51*, 2309–2315. [CrossRef]
18. Heki, K. Ionospheric electron enhancement preceding the 2011 Tohoku-Oki earthquake. *Geophys. Res. Lett.* **2011**, *38*, L17312. [CrossRef]
19. Sharma, G.; Nayak, K.; Romero-Andrade, R.; Mohammed-Aslam, M.A.; Sarma, K.K.; Aggarwal, S.P. Low Ionosphere Density Above the Earthquake Epicentre Region of Mw 7.2, El Mayor–Cucapah Earthquake Evident from Dense CORS Data. *J. Indian Soc. Remote. Sens.* **2024**, *52*, 543–555. [CrossRef]
20. Tachema, A.; Nadji, A. Geodetic contribution to predict the seismological activity of the Italian metropolis by the ionospheric variant of GPS_TEC. *J. Atmos. Sol. Terr. Phys.* **2019**, *183*, 1–10. [CrossRef]
21. Nayak, K.; López-Urías, C.; Romero-Andrade, R.; Sharma, G.; Guzmán-Acevedo, G.M.; Trejo-Soto, M.E. Ionospheric Total Electron Content (TEC) Anomalies as Earthquake Precursors: Unveiling the Geophysical Connection Leading to the 2023 Moroccan 6.8 Mw Earthquake. *Geosciences* **2023**, *13*, 319. [CrossRef]
22. Haider, S.F.; Shah, M.; Li, B.; Jamjareegulgarn, P.; de Oliveira-Júnior, J.F.; Zhou, C. Synchronized and Co-Located Ionospheric and Atmospheric Anomalies Associated with the 2023 Mw 7.8 Turkey Earthquake. *Remote Sens.* **2024**, *16*, 222. [CrossRef]
23. Baubron, J.C.; Rigo, A.; Toutain, J.P. Soil gas profiles as a tool to characterize active tectonic areas: The Jaut Pass example (Pyrenees, France). *Earth Planet. Sci. Lett.* **2002**, *196*, 69–81. [CrossRef]
24. Fu, C.C.; Yang, T.F.; Walia, V.; Chen, C.-H. Reconnaissance of soil gas composition over the buried fault and fracture zone in southern Taiwan. *Geochem. J.* **2005**, *39*, 427–439. [CrossRef]
25. Fu, C.C.; Yang, T.F.; Chen, C.H.; Lee, L.C.; Wu, Y.M.; Liu, T.K.; Walia, V.; Kumar, A.; Lai, T.H. Spatial and temporal anomalies of soil gas in northern Taiwan and its tectonic and seismic implications. *J. Asian Earth Sci.* **2017**, *149*, 64–77. [CrossRef]
26. Walia, V.; Yang, T.F.; Hong, W.L.; Lin, S.J.; Fu, C.C.; Wen, K.L.; Chen, C.H. Geochemical variation of soil-gas composition for fault and earthquake precursory studies along Hsincheng fault in NW Taiwan. *Appl. Radiat. Isot.* **2009**, *67*, 1855–1863. [CrossRef]
27. Woith, H. Radon earthquake precursor: A short review. *Eur. Phys. J. Spec. Top.* **2015**, *224*, 611–627. [CrossRef]
28. Yuce, G.; Fu, C.C.; D'Alessandro, W.; Gulbay, A.H.; Lai, C.W.; Bellomo, S.; Yang, T.F.; Italiano, F.; Walia, V. Geochemical characteristics of soil radon and carbon dioxide within the Dead Sea Fault and Karasu Fault in the Amik Basin (Hatay), Turkey. *Chem. Geol.* **2017**, *469*, 129–146. [CrossRef]
29. Chen, Z.; Li, Y.; Liu, Z.; He, H.; Martinelli, G.; Lu, C.; Gao, Z. Geochemical and geophysical effects of tectonic activity in faulted areas of the North China Craton. *Chem. Geol.* **2022**, *609*, 121048. [CrossRef]
30. Li, Y.; Chen, Z.; Sun, A.; Liu, Z.; Caracausi, A.; Martinelli, G.; Lu, C. Geochemical features and seismic imaging of the tectonic zone between the Tibetan Plateau and Ordos Block, central northern China. *Chem. Geol.* **2023**, *622*, 121386. [CrossRef]
31. Cui, Y.J.; Li, Y.; Zheng, W.; Huang, J.N.; Zeng, Z.J.; Liu, Z.F.; Zhou, X.C.; Sun, F.X.; Zou, Z.Y.; Si, X.Y.; et al. CH_4 and CO_2 emissions from different tectonic settings along the western margin of the Ordos Block in China: Output and correlation with the regional tectonics. *Geochem. Geophys. Geosyst.* **2024**, *25*, e2024GC011661. [CrossRef]
32. Freund, F. Pre-earthquake signals: Underlying physical processes. *J. Asian Earth Sci.* **2011**, *41*, 383–400. [CrossRef]
33. Heinicke, J.; Koch, U.; Martinelli, G. CO_2 and Radon measurements in the Vogtland area (Germany)—A contribution to earthquake prediction research. *Geophys. Res. Lett.* **1995**, *22*, 771–774. [CrossRef]

34. Walia, V.; Virk, H.S.; Bajwa, B.S. Radon precursory signals for some earthquakes of magnitude > 5 occurred in N-W Himalaya. *Pure Appl. Geophys.* **2006**, *163*, 711–721. [CrossRef]
35. Miklavčić, I.; Radolić, V.; Vuković, B.; Poje, M.; Varga, M.; Stanić, D.; Planinić, J. Radon anomaly in soil gas as an earthquake precursor. *Appl. Radiat. Isot.* **2008**, *66*, 1459–1466. [CrossRef]
36. Igarashi, G.; Saeki, S.; Takahata, N.; Sano, Y. Ground-Water Radon Anomaly Before the Kobe Earthquake in Japan. *Science* **1995**, *269*, 60–61. [CrossRef]
37. Kawada, Y.; Nagahama, H.; Omori, Y.; Yasuoka, Y.; Ishikawa, T.; Tokonami, S.; Shinogi, M. Time-scale invariant changes in atmospheric radon concentration and crustal strain prior to a large earthquake, Nonlin. *Process. Geophys.* **2007**, *14*, 123–130. [CrossRef]
38. Wasteby, N.; Skelton, A.; Tollefsen, E.; Andrén, M.; Stockmann, G.; Liljedahl, L.C.; Sturkell, E.; Morth, M. Hydrochemical monitoring, petrological observation, and geochemical modeling of fault healing after an earthquake. *J. Geophys. Res.-Solid Earth* **2014**, *119*, 5727–5740. [CrossRef]
39. Zhao, Y.; Liu, Z.; Li, Y.; Hu, L.; Chen, Z.; Sun, F.; Lu, C. A case study of 10 years groundwater radon monitoring along the eastern margin of the Tibetan Plateau and in its adjacent regions: Implications for earthquake surveillance. *Appl. Geochem.* **2021**, *131*, 105014. [CrossRef]
40. Yang, T.F.; Fu, C.C.; Walia, V.; Chen, C.H.; Chyi, L.L.; Liu, T.K.; Song, S.R.; Lee, M.; Lin, C.W.; Lin, C.C. Seismo-geochemical variations in SW Taiwan: Multiparameter automatic gas monitoring results. *Pure Appl. Geophys.* **2006**, *163*, 693–709. [CrossRef]
41. Fu, C.C.; Lai, C.W.; Yang, T.F.; Hilton, D.R.; Chen, C.H.; Walia, V.; Kumar, A.; Lee, L.C. An automatic system for continuous monitoring and sampling of groundwater geochemistry in earthquake-prone regions of SW Taiwan. *Front. Earth Sci.* **2021**, *9*, 635913. [CrossRef]
42. Kuo, M.C.T.; Fan, K.; Kuochen, H.; Chen, W. A Mechanism for anomalous decline in radon precursory to an earthquake. *Ground Water* **2006**, *44*, 642–647. [CrossRef] [PubMed]
43. Kuo, M.C.T.; Chen, W.; Ho, C. Anomalous decrease in groundwater radon before 2016 M_w 6.4 Meinong earthquake and its application in Taiwan. *Appl. Radiat. Isot.* **2018**, *136*, 68–72. [CrossRef] [PubMed]
44. Walia, V.; Lin, S.J.; Hong, W.L.; Fu, C.C.; Yang, T.F.; Wen, K.L.; Chen, C.H. Continuous temporal soil-gas composition variations for earthquake precursory studies along Hsincheng and Hsinhua faults in Taiwan. *Radiat. Meas.* **2009**, *44*, 934–939. [CrossRef]
45. Walia, V.; Yang, T.F.; Lin, S.J.; Kumar, A.; Fu, C.C.; Chiu, J.M.; Chang, H.H.; Wen, K.L.; Chen, C.H. Temporal variation of soil gas compositions for earthquake surveillance in Taiwan. *Radiat. Meas.* **2013**, *50*, 154–159. [CrossRef]
46. Chyi, L.L.; Quick, T.J.; Yang, F.T.; Chen, C.H. The origin and detection of spike-like anomalies in soil gas radon time series. *Geochem. J.* **2011**, *45*, 431–438. [CrossRef]
47. Kumar, A.; Walia, V.; Arora, B.R.; Yang, T.F.; Lin, S.J.; Fu, C.C.; Chen, C.-H.; Wen, K.L. Identifications and removal of diurnal and semidiurnal variations in radon time series data of Hsinhua monitoring station in SW Taiwan using singular spectrum analysis. *Nat. Hazards* **2015**, *79*, 317–330. [CrossRef]
48. Fu, C.C.; Wang, P.K.; Lee, L.C.; Lin, C.H.; Chang, W.Y.; Giuliani, G.; Ouzounov, D. Temporal variation of gamma rays as a possible precursor of earthquake in the Longitudinal Valley of eastern Taiwan. *J. Asian Earth Sci.* **2015**, *114*, 362–372. [CrossRef]
49. Fu, C.C.; Lee, L.C.; Yang, T.F.; Lin, C.H.; Chen, C.H.; Walia, V.; Liu, T.K.; Ouzounov, D.; Giuliani, G.; Lai, T.H.; et al. Gamma ray and radon anomalies in northern Taiwan as a possible preearthquake indicator around the plate boundary. *Geofluids* **2019**, *2019*, 4734513. [CrossRef]
50. Giuliani, G.; Attanasio, A.; Fioravanti, G. Gamma detectors for continuous monitoring of radon. *J. Int. Environ. Appl. Sci.* **2013**, *8*, 541–550.
51. Liu, J.Y.; Chen, Y.I.; Pulinets, S.A.; Tsai, Y.B.; Chuo, Y.J. Seismo-ionospheric signatures prior to M 6.0 Taiwan earthquakes. *Geophys. Res. Lett.* **2000**, *27*, 3113–3116. [CrossRef]
52. Tsai, T.C.; Jhuang, H.K.; Ho, Y.Y.; Lee, L.C.; Su, W.C.; Hung, S.L.; Lee, K.H.; Fu, C.C.; Lin, H.C.; Kuo, C.L. Deep learning of detecting ionospheric precursors associated with M $\geq$ 6.0 earthquakes in Taiwan. *Earth Space Sci.* **2022**, *9*, e2022EA002289. [CrossRef]
53. Liu, J.Y.; Chen, Y.I.; Chuo, Y.J.; Chen, C.S. A statistical investigation of preearthquake ionospheric anomaly. *J. Geophys. Res.* **2006**, *111*, A05304. [CrossRef]
54. Takeyasu, M.; Iida, T.; Tsujimoto, T.; Yamasaki, K.; Ogawa, Y. Concentrations and their ratio of ^{222}Rn decay products in rainwater measured by gamma-ray spectrometry using a low-background Ge detector. *J. Environ. Radioact.* **2006**, *88*, 74–89. [CrossRef]
55. Livesay, R.; Blessinger, C.S.; Guzzardo, T.; Hausladen, P. Rain-induced increase in background radiation detected by Radiation Portal Monitors. *J. Environ. Radioact.* **2014**, *137*, 137–141. [CrossRef] [PubMed]
56. Melintescu, A.; Chambers, S.; Crawford, J.; Williams, A.; Zorila, B.; Galeriu, D. Radon-222 related influence on ambient gamma dose. *J. Environ. Radioact.* **2018**, *189*, 67–78. [CrossRef]
57. Pulinets, S.; Ouzounov, D. Lithosphere-Atmosphere-Ionosphere Coupling (LAIC) model—An unified concept for earthquake precursors validation. *J. Asian Earth Sci.* **2011**, *41*, 371–382. [CrossRef]

58. Kobeissi, M.A.; Gomez, F.; Tabet, C. Measurement of Anomalous Radon Gas Emanation Across the Yammouneh Fault in Southern Lebanon: A Possible Approach to Earthquake Prediction. *Int. J. Disaster Risk Sci.* **2015**, *6*, 250–266. [CrossRef]
59. Oh, Y.H.; Kim, G. A radon-thoron isotope pair as a reliable earthquake precursor. *Sci. Rep.* **2015**, *5*, 13084. [CrossRef]
60. Asencio-Cortés, G.; Martínez Álvarez, F.; Troncoso, A.; Morales-Esteban, A. Medium–large earthquake magnitude prediction in Tokyo with artificial neural networks. *Neural Comput. Appl.* **2017**, *28*, 1043–1055. [CrossRef]
61. Asim, K.M.; Idris, A.; Iqbal, T.; Martinez-Alvarez, F. Earthquake prediction model using support vector regressor and hybrid neural networks. *PLoS ONE* **2018**, *13*, e0199004. [CrossRef]
62. Tramutoli, V.; Aliano, C.; Corrado, R.; Filizzola, C.; Genoano, N.; Lisi, M.; Martinelli, G.; Pergola, N. On the possible origin of thermal infrared radiation (TIR) anomalies in earthquake-prone areas observed using robust satellite techniques (RST). *Chem. Geol.* **2013**, *339*, 157–168. [CrossRef]
63. Fu, C.C.; Lee, L.C.; Ouzounov, D.; Jan, J.C. Earth's outgoing longwave radiation variability prior to M $\geq$ 6.0 earthquakes in the Taiwan area during 2009–2019. *Front. Earth Sci.* **2020**, *8*, 364. [CrossRef]
64. Gutenberg, B.; Richter, C.F. Frequency of earthquakes in California. *Bull. Seism. Soc. Am.* **1944**, *34*, 185–188. [CrossRef]
65. Chan, C.H.; Kao, J.C.; Chen, D.Y. Spatial-temporal variations of b-values prior to medium-to-large earthquakes in Taiwan and the feasibility of real-time precursor monitoring. *Earth Planets Space* **2024**, *76*, 119. [CrossRef]
66. Chen, S.K.; Chen, P.Y.; Wu, Y.M.; Chen, C.C.; Chan, C.H. Temporal variations of earthquake magnitude-frequency relation in the source area of M $\geq$ 6.0 earthquakes: A systematic survey in Taiwan. *Earth Space Sci.* **2023**, *10*, e2023EA002927. [CrossRef]
67. Chen, C.R.; Liu, J.Y.; Chen, C.H.; Wu, T.Y.; Yen, H.Y.; Wen, S.; Huang, B.S.; Lin, C.H.; Lin, C.M.; Hsieh, H.H. Co-seismic geomagnetic fluctuations and atmospheric disturbances during the 2018 M 6.2 Hualien Earthquake. *Terr. Atmos. Ocean. Sci.* **2019**, *30*, 449–465. [CrossRef]
68. Freund, F. Time-resolved study of charge generation and propagation in igneous rocks. *J. Geophys. Res.* **2000**, *105*, 11001–11020. [CrossRef]
69. Freund, F. Toward a unified solid state theory for pre-earthquake signals. *Acta Geophys.* **2010**, *58*, 719–766. [CrossRef]
70. Kuo, C.L.; Huba, J.; Joyce, G.; Lee, L.C. Ionosphere plasma bubbles and density variations induced by pre-earthquake rock currents and associated surface charges. *J. Geophys. Res.* **2011**, *116*, A10317. [CrossRef]
71. Kuo, C.L.; Lee, L.C.; Huba, J.D. An improved coupling model for the lithosphere-atmosphere-ionosphere system. *J. Geophys. Res. Space Phys.* **2014**, *119*, 3189–3205. [CrossRef]
72. Sorokin, V.M.; Hayakawa, M. Generation of seismic-related DC electric fields and lithosphere-atmosphere-ionosphere coupling. *Mod. Appl. Sci.* **2013**, *7*, 6. [CrossRef]
73. Shalimov, S.L.; Gokhberg, M.B. Lithosphere-ionosphere coupling mechanism and its application to the earthquake in Iran on June 20, 1990. A review of ionospheric measurements and basic assumptions. *Phys. Earth Planet. Inter.* **1998**, *105*, 211–218. [CrossRef]
74. Orihara, Y.; Kamogawa, M.; Nagao, T. Preseismic Changes of the Level and Temperature of Confined Groundwater related to the 2011 Tohoku Earthquake. *Sci. Rep.* **2014**, *4*, 6907. [CrossRef]
75. Nakajima, J.; Uchida, N. Repeated drainage from megathrust during episodic slow slip. *Nat. Geosci.* **2018**, *11*, 351–356. [CrossRef]
76. Lee, S.J.; Lin, T.C.; Liu, T.Y.; Wong, T.P. Fault-to-fault jumping rupture of the 2018 Mw 6.4 Hualien earthquake in eastern Taiwan. *Seismo. Res. Lett.* **2018**, *90*, 30–39. [CrossRef]

Disclaimer/Publisher's Note: The statements, opinions and data contained in all publications are solely those of the individual author(s) and contributor(s) and not of MDPI and/or the editor(s). MDPI and/or the editor(s) disclaim responsibility for any injury to people or property resulting from any ideas, methods, instructions or products referred to in the content.